Industrial Chemistry & Materials

ROYAL SOCIETY OF CHEMISTRY

PAPER

View Article Online
View Journal

Cite this: DOI: 10.1039/d5im00219b

Single-atom magnesium promoter to boost solar-driven hydrogen photoproduction

Esperanza Fernández-García,[a] Uriel Caudillo-Flores,[b] Rocío Sayago-Carro,[a] A. Tolosana-Moranchel,[a] Marcos Fernández-García *[a] and Anna Kubacka *[a]

Received 26th August 2025,
Accepted 31st October 2025

DOI: 10.1039/d5im00219b

rsc.li/icm

Enhancing the performance of titania-based systems has emerged as a central goal to allow the light-triggered continuous production of hydrogen using renewable energy and bio-based sacrificial molecules. A cheap and widely available promoter based on magnesium is here exploited to provide a long-term stable catalytic response and maximize the formation of hydrogen. Using the International Union of Pure and Applied Chemistry (IUPAC)-recommended quantum efficiency as the parameter to measure activity, this study demonstrates an 8.2-fold increase in photocatalytic activity compared with the Pt–TiO_2 reference catalyst, achieving a quantum efficiency of 3.0% under sunlight. The physicochemical study provides evidence that the increase in activity is achieved through a precise synthesis procedure, resulting in the formation of atom-dispersed Mg(II) entities. The origin of the promotion effect appears to be related to the reaction mechanism, with a limited effect from charge carrier generation or recombination. An *in situ* infrared study showed that the surface effects connected to the adsorption of alcohol, as well as the generation and (subsequent) evolution of bridge carbonate species, appear at the core of the enhancement in activity. The magnesium promoter, spread as single-atom entities over titania, is thus shown as a way to obtain highly active and stable photocatalytic systems for green hydrogen production.

Keywords: Single-atom promoter; Sunlight; Quantum efficiency; Mechanism; Hydrogen.

1 Introduction

Production of hydrogen using renewable energy and reactant resources is essential for approaching a future with net-zero carbon emissions, environmentally respectful and safe for humans.[1–3] Green alternatives for hydrogen production are urgently needed to satisfy the growing demand from industrial processes such as hydrocarbon and plastics manufacturing, as well as from its use as fuel in transportation and in hydrogen-fed fuel cells.[4] Thus, novel methods for hydrogen production are actively being explored and are expected to provide the foundation for fulfilling the growing demand for this chemical. Contributions from the photocatalysis field, particularly using sunlight as an energy source and bio-based molecules as a hydrogen source, would be welcomed in this context. Nevertheless, the potential of such technology is nowadays limited by several factors, among which a key issue concerns the relatively low efficiency of the reaction, irrespective of the catalyst used. If solar light is used as the primary excitation energy, addressing this challenge requires simultaneously enhancing the activity of the catalyst(s) under (at least) the UV and visible regions of the solar spectrum.[5,6]

Titania is the most explored material as a photocatalyst. Its performance has been shown to be outstanding in many fields, including hydrogen production. Ways of improving titania-based materials continue to be actively investigated. The main weaknesses of titania-based catalysts relate to several physicochemical issues. Light-related ones concern limited absorption of visible light due to a 3.0–3.2 eV band gap, as well as improvable control over charge carrier recombination. Light and chemical limiting issues encountered at the reactive surface of titania are primarily related to the trapping of charge carrier species by different surface species, such as hydroxyl and vacancies, as well as the interaction of such surface radical species with the chemicals involved in the desired reaction, controlling reaction mechanism and kinetics.[1–3] For hydrogen production, a key beneficial effect arises from the use of a cocatalyst, with platinum consistently delivering the best performance. Pt is known to play an active chemical role in the reaction and limits charge recombination by capturing electrons and increasing their lifetime with the help of the adequate electronic properties of the Pt–titania interface.[7–9] In addition, the structural/electronic modification of titania

[a] Instituto de Catálisis y Petroleoquímica, CSIC, C/Marie Curie 2, 28049-Madrid, Spain. E-mail: mfg@icp.csic.es, ak@icp.csic.es
[b] Centro de Nanociencias y Nanotecnología, Universidad Nacional Autónoma de México, Ensenada 22800, Mexico

by metals and non-metals has been extensively explored. Many metals have been tested, but particular efforts have been devoted to enhancing and controlling light absorption and charge recombination through either doping at the bulk or the use of surface species as atomic or molecular entities. The alteration of the electronic structure, particularly the valence-conduction bands and band gap energy, together with the presence of defect-related gap-localized electronic states, are commonly claimed as key factors for the improvement in activity. In addition, changes in surface connections with redox and acid–base properties are commonly pointed out as critical to obtain high activity.[9–12] The resulting landscape portrays composite metal–support systems as novel top catalysts with co-catalysts and/or surface species, as well as doping species, shaping the performance of the titania-based materials. Often, such complex catalysts have specific nanostructures and/or interfaces that may be complex to maintain under reaction, particularly considering the long-term on-stream requirement for practical application.[7,13–16]

For cocatalyst or surface species, single-atom entities are actively sought to boost activity for hydrogen photoproduction. Nevertheless, small nanoparticles of Pt deposited on titania would show improved performance when compared with isolated and subnanometric species.[17] A careful inspection of hydrogen photon production using turnover frequencies (TOF) and quantum efficiency (QE) is required to provide a clear answer to this point.[18,19] The physicochemical grounds for such behavior can be strongly related to chemical effects (oxidation state of the noble metal) as well as the size-dependence of electron capture and subsequent charge recombination on platinum entities. In addition, note that the TOF and QE values for single-atom and (sub- or nanometric) cluster entities cannot, on their own, determine the average (macroscopic) values observed in a catalyst. In addition to the single-particle TOF and QE values, the corresponding macroscopic values would be determined by the population density of the different species present in a real catalyst, as well as stability issues. In this context, note that the long-term stability of the isolated platinum species on titania is dubious under (hydrogen photoproduction) reaction conditions due to agglomeration and/or leaching.[9] A different situation may occur in the case of promoters with strong interaction with titania. Cationic metal-based species able to provide stable oxidic environments are typical promoters of titania.[1–3,11,20] The enhancement in photoactivity has been shown to be significant in the case of (transition and rare-earth metal) single-atom entitites.[21,22]

Our manuscript attempts to screen a cheap and widely available promoter, such as magnesium at the surface of an anatase system, with platinum as a cocatalyst. Magnesium has been shown to provide activity as a doping agent[23] or surface promoter.[24] However, as shown below, the activity enhancement presented in these studies is limited. Following the IUPAC recommendations and using the quantum efficiency parameter,[25] we will show an outstanding and stable promoting effect due to isolated magnesium species located on the catalyst surface. The use of a single-atom promoter is thus described as a rather useful tool to enhance the activity of well-known systems such as Pt-cocatalyst titania-based solids.

2 Results and discussion

2.1 Characterization

The chemical composition of the solids was examined with inductively coupled plasma atomic absorption spectroscopy (ICP-OES). Table S1 collects the corresponding results, confirming that real catalysts contain the expected magnesium and platinum loadings within an error of *ca.* 5.3%. Fig. 1 displays TEM images of selected catalysts. The TEM images (Fig. 1a, b, d, e, g and h) reveal the presence of darker entities supported over larger platelets. According to the interplanar distance values obtained from the processing of the images (0.221 nm), the darker entities correspond to Pt(0) nanoparticles, characterized in most cases by the pattern corresponding to the (111) closed packing plane. Analysis of the Feret diameter for the platinum nanoparticles provides the particle size distribution presented in Fig. 1c, f and i. These distributions have relatively similar average particle size distributions. The average primary particle size is constant throughout all the samples in the series (*ca.* 3.0 nm, as summarized in Table S2). Moreover, the particle size distribution is always relatively narrow (from *ca.* 0.5 to 3.5 nm). Although some differences can be observed in the high-order moments (skewness and kurtosis) of the distributions, analysis of the dispersion leads to rather similar dispersion values for all samples (Table S2). Thus, the fraction of Pt atoms at the surface of the catalysts is essentially constant in the series under study.

The larger entities displayed in the HR-TEM (high-resolution transmission electron microscopy) images correspond to titania nanoplatelets, showing the (101) basal plane of the anatase polymorph. This polymorph dominates the XRD (X-ray diffraction) patterns for all the Pt*x*Mg (where *x* is the molar content of Mg; see section 4) and reference samples (Fig. 1j). From low to high two-theta angle values in the XRD patterns of all samples, we can see the (101) peak at *ca.* 25.11°, the (103), (004), (102) triplet centered at *ca.* 37.74°, the (200) peak at 47.83°, the (105) peak at 54.04°, the (211) peak at 54.74°, the (204) peak at 62.51°, and other minor peaks at higher angles. As discussed before, all these peaks can be ascribed to the anatase phase with $I4_1/amd$ space group (JCPDS card 01-084-1286).[26] The primary particle size of the anatase obtained from XRD is also relatively similar for all catalysts. Table S3 includes the corresponding values, which go from *ca.* 10.7 nm for the PtT (platinum–titania) sample to 8.5 nm for the Pt7.5Mg solid. The presence of magnesium modestly decreases the crystallite size of the anatase nanoplatelets. The table provides evidence that Pt

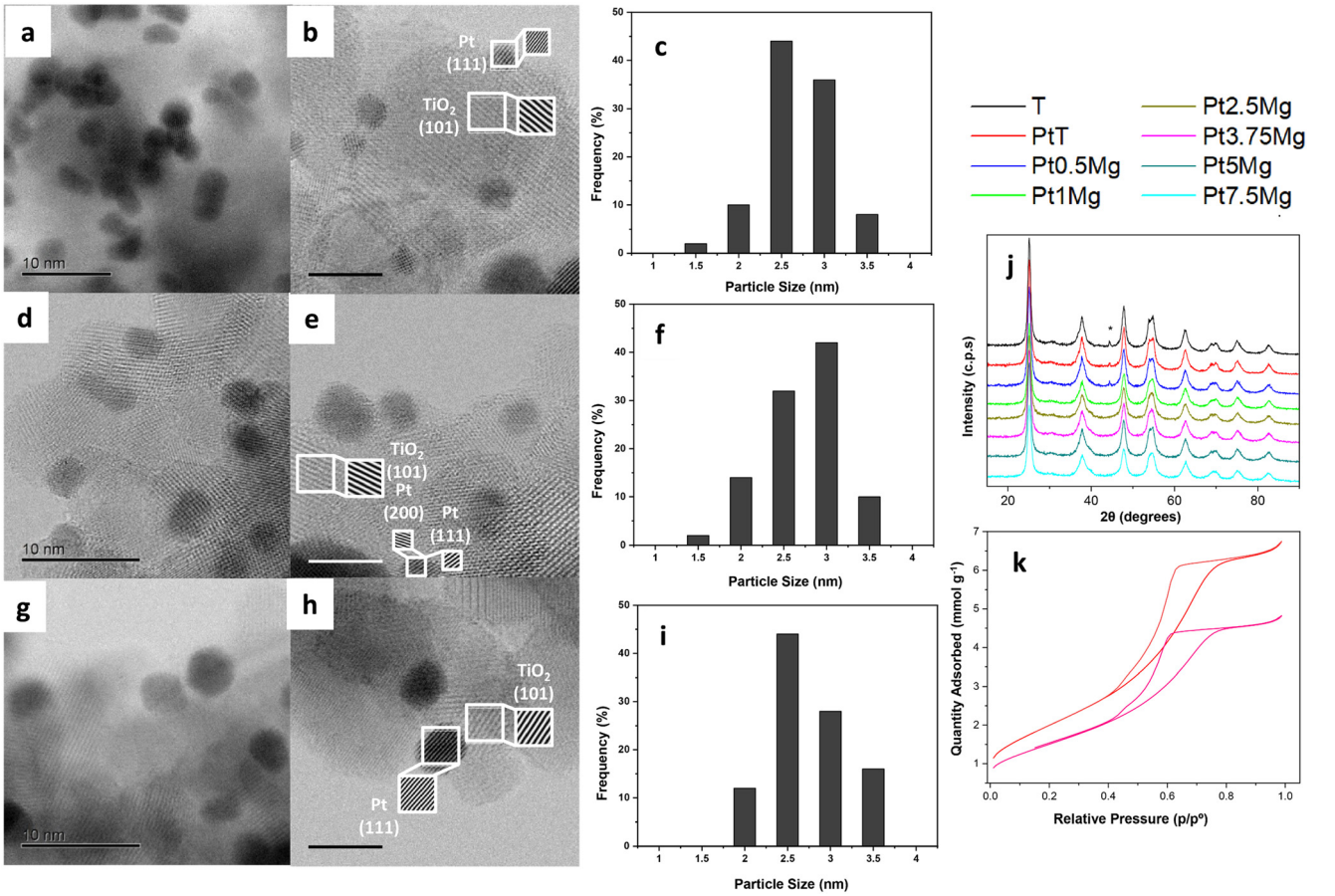

Fig. 1 HR-TEM images and platinum particle size distribution for PtT (a–c), Pt3.75Mg (d–f) and Pt7.5Mg (g–i) samples; (j and k) display XRD patterns and nitrogen isotherm results, respectively, for selected samples. The asterisk in Fig. 1j marks a contribution from the sample holder.

deposition has a relatively minor effect on anatase, as may be expected from the preparation procedure.

Textural and morphological properties of the catalysts were further investigated. Nitrogen adsorption/desorption isotherm profiles for selected samples are presented in Fig. 1k as representative examples. All the solids are mesoporous materials, owing to a characteristic H4 type loop dominated by adsorbate–solid interactions.[27] BET (Brunauer–Emmett–Teller) surface area values are collected in Table S3. This parameter shows values ranging from *ca.* 125 to 165 $m^2\ g^{-1}$, and increases smoothly from the PtT to the Pt7.5Mg samples. The inverse correlation between the primary particle size (crystallite size obtained from XRD) and BET area indicates that morphological differences between samples are mainly attributable to the variations in the former parameter. However, such differences are rather modest, as all samples are mesoporous materials with high surface area (over 125 $m^2\ g^{-1}$).

Additional information about the minor components of the catalysts was obtained through the use of dark-field STEM microscopy. Fig. 2a shows a high-magnification view in which the (mostly) isolated ions are clearly detected on the anatase surface of the Pt3.75Mg sample. Very few aggregation entities of no more than 3 atoms are observed. Moreover, the EDS (X-ray energy dispersive analysis) analysis of a larger portion of the material provides evidence of the high dispersion of such entities. The presence of the (dominant) isolated single-atom entities is observed in all magnesium-containing samples using dark-field STEM. Note that such entities are absent in the STEM micrographs of the PtT reference sample (Fig. S1). The chemical nature of the single-atom species can be ascribed unequivocally by comparing the microscopic analysis of the T and 3.75Mg support solids presented in Fig. S2a–e. These entities are observed in both the bright- and dark-field microscopy images of the magnesium-containing support (Fig. 2c–e). They are located at surface positions but are absent on the T material, indicating that they can be observed only in the presence of magnesium in the support powders. Fig. S2d shows that such single-atom entities occupied surface positions out of the anatase (TiO_2) crystallographic planes. These two observations strongly suggest that such entities differ chemically relative to the atoms located at anatase planes. The assignment to magnesium single-atom entities would thus be evident. EDS analysis provides evidence of the high dispersion of the atomic-size magnesium entities, achieved with our preparation method in all (magnesium-containing) Pt*x*Mg samples in the series (Fig. S3). Further evidence of the

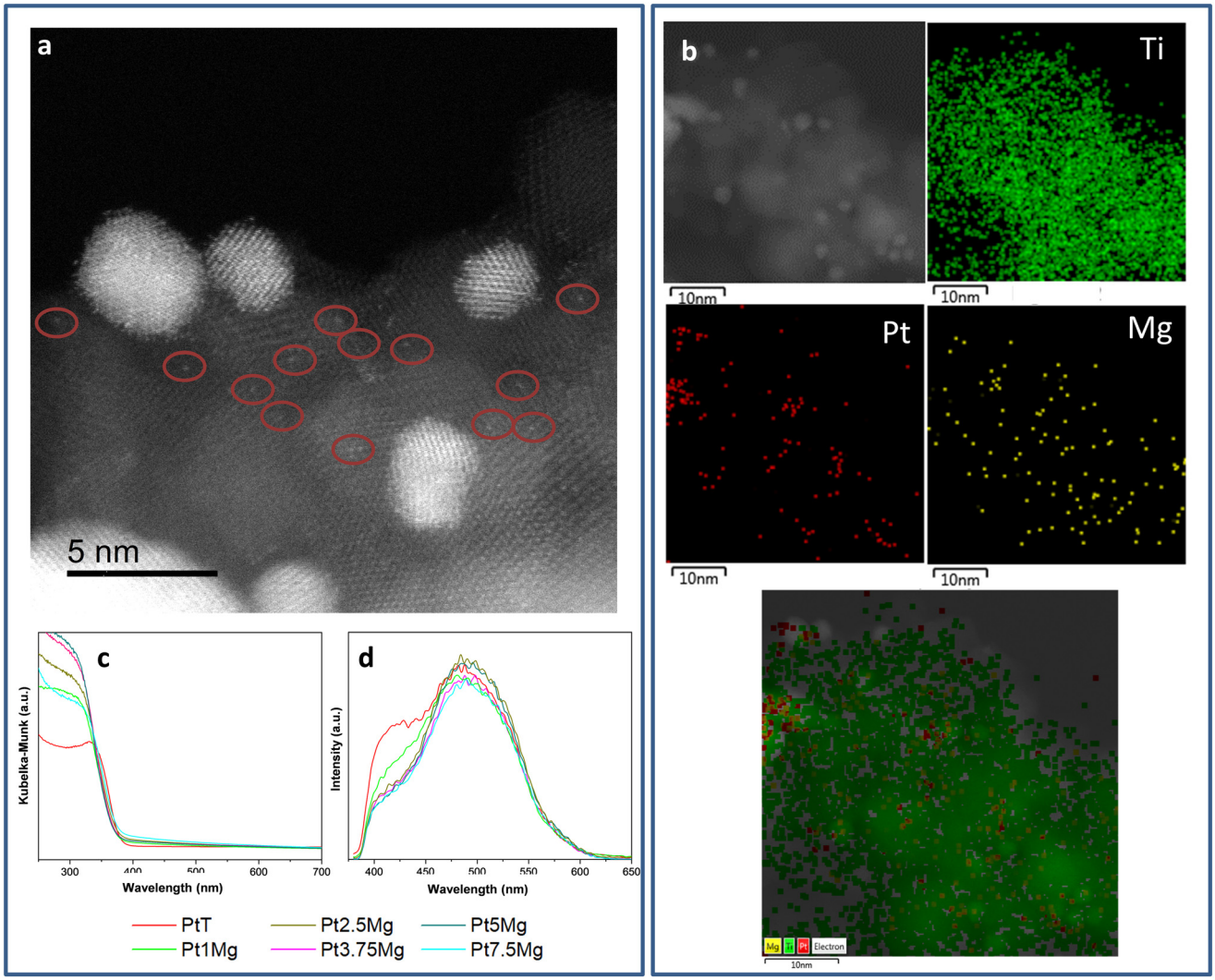

Fig. 2 (a) Dark-field HR-STEM for the Pt3.75Mg sample. Circles highlight magnesium entities; (b) dark-field STEM and EDS mapping for the Pt3.75Mg sample; (c) UV-visible, and (d) photoluminescence spectra for the samples.

good dispersion achieved comes from a comparison with a support having the same magnesium content (3.75 mol%) and prepared using a conventional impregnation method. The differences in magnesium dispersion are evident (Fig. S2). In this context, it can be noted that the invariance observed in the position of anatase-related XRD peak(s) (Fig. 1j) is in accordance with the dominant surface position of magnesium at the anatase, with any doping effect being negligible.

Further information about the effect of magnesium on physicochemical properties of the solids was obtained through the measurement of the optoelectronic properties with the help of UV-visible and photoluminescence spectroscopies. UV-visible spectra (Fig. 2c) are dominated by the main (by weight) anatase component. An S-type shape is observed, demonstrating the semiconductor nature of the anatase. Anatase is, as mentioned earlier, an indirect gap semiconductor,[28] and the band gap values of the samples obtained are also reported in Table S3. A roughly constant value of 3.1 to 3.3 eV is obtained for all samples, a value characteristic of the anatase polymorph.[11] Additionally, a flat, ill-defined tail extending throughout the visible region (up to *ca.* 550 nm) of the spectra is also detected. This is commonly attributed to lattice vacancies, which seem to grow with the Mg content.[11,29] The photoluminescence spectra allow analysis of the defect states. Under UV excitation, defect-related states (particularly anion-related defects in the case of anatase) contribute to anatase de-excitation. Anatase-based systems normally present two well-differentiated de-excitation processes, called green and red, as shown in Fig. 2d. These bands are connected with band-to-defect-related electronic transitions, the green one sampling defects near the conduction band and the red one near the valence band.[30,31] The photoluminescence signal shows a consistent decrease in intensity relative to the PtT reference. This happens irrespective of the excitation wavelength. This fact strongly suggests that the tail observed in the UV-visible spectra would be related to near-band, edge-type localized

electronic states.[32,33] In this case, surface states associated with magnesium in strong interaction with anatase create small distortions in the density of states at the edge of the conduction/valence bands. Although the corresponding density of states is rather small, these electronic states allow light absorption in the visible range. The study of the optoelectronic properties was carried out using linear potential sweep photoresponse experiments (Fig. S4). They show that, when the light was off, no current was detected. Conversely, when the photoelectrodes were irradiated, for most of the catalysts, the photoresponse density increased almost linearly upon increasing the applied potentials from 0 to 0.8 V *vs.* Ag/AgCl. However, exponential growth was noted at higher potential. Such positive current densities are ascribed to the oxygen evolution reaction (OER) under irradiation and can be used to evaluate their activity. The Pt5Mg photocatalysts yielded the greatest photoresponse density (65 μA cm^{-2} at 0.75 V *vs.* Ag/AgCl), followed by Pt3.75Mg, Pt2.5Mg and Pt1Mg, which provided similar values (around 51 μA cm^{-2} at 0.75 V *vs.* Ag/AgCl). Regardless of the Mg concentration, all the photocatalysts performed better than PtT at potentials above 0.25 V *vs.* Ag/AgCl. These results confirm the improved charge separation displayed in the presence of magnesium, which entails longer electron lifetimes. The decrease in photoresponse observed for the photocatalyst with the highest Mg concentration (33 μA cm^{-2} at 0.75 V *vs.* Ag/AgCl), Pt7.5Mg, could be due to changes in the above-detected defect-related states that lead to a slow electron–hole separation rate.[34,35]

XPS (X-ray photoelectron spectroscopy) was used to further analyze the electronic effects connected with the presence of the defects detected in the UV-vis and photoluminescence studies. The O1s peak contains information about several oxygen species, *e.g.*, lattice oxygen, defects and surface species, mainly OH and adsorbed H_2O.[36,37] Fig. S5 schematically shows the binding energy regions of these three species using the PtT sample. In the figure, the overlap between the last two mentioned oxygen-containing species is highlighted (in color). In any case, the modest growth of the intensity in the 531–532 eV region is in line with the above results. A similar conclusion can be obtained by detailed analysis of the valence band of the solids and the electronic states observed above its edge (Fig. S5). Therefore, certain mild growth of defects with the magnesium content is observed, although such growth does not display simple behavior or correlation with magnesium content. Moreover, analysis of the valence band evidences the lack of differences in the top-edge energy between the samples (Fig. S5). The constant band gap value on the samples (Table S3) indicates the relatively limited changes in valence and conduction band positions (particularly for samples with an Mg molar content below or equal to 5%) throughout the series of samples studied.

In summary, the analysis of defect structures using XPS, photoluminescence, and photoresponse measurements indicates that magnesium promotes the generation of (mainly) oxygen-associated defect states in the Pt*x*Mg samples, although the extent of these defects does not show an obvious correlation with magnesium content. We would like to remark that the observed decrease in photoluminescence intensity in the presence of magnesium would promote the number of charge carrier species and the charge carrier lifetime. As a result, the probability of a charge carrier reaching the surface and its involvement in the chemical steps of photocatalytic processes both increase.[30,38] Apart from that, rather limited changes are observed in other electronic properties, particularly the band-edge position of the valence and conduction bands.

The physicochemical characterization of the platinum- and magnesium-containing components was completed using XPS analysis. First, we note that the commonly scanned Pt 4f is distorted by the Ti plasmon peak in the presence of anatase.[36,39] For this reason, we also scanned the Pt 4d peak. As shown in Fig. S6, the Pt $4f_{7/2}$ and Pt $4d_{5/2}$ XPS signals display binding energies at 70.4 and 313.8 eV, respectively. They are both characteristic of metallic platinum species.[36] A key point is that the signal (intensity and binding energy) is essentially invariant throughout the series of samples. In agreement with the microscopic study, the average particle sizes of the Pt(0) nanoparticles present in the samples of the series do not show significant differences. The Mg 1s XPS peak was also recorded for our samples (Fig. S7). The Mg 2p XPS peak has limited utility due to its strong overlap with Pt $5p_{3/2}$ XPS peaks.[36] The limited occupancy of the 1s orbital (two electrons), as well as the limited absorption coefficient for single-atom magnesium entities, would make the signal relatively weak, yet, as expected, the intensity grows with the magnesium content of the material, as was previously discussed in light of other techniques (Fig. S7). In addition, the 1 s Mg XPS peak displays a constant binding energy throughout the series of *ca.* 1304.2 eV. This binding energy is characteristic of Mg(II) species in oxidic environments.[36]

Finally, the acidity and basicity of the catalysts were studied using thermo-programmed desorption experiments with NH_3 and CO_2 as probe molecules, respectively. Fig. S8 shows the results of the aforementioned tests. The adsorption capability of the solids is customarily analyzed in terms of the low, medium and high adsorption strength fractions. This physicochemical parameter, adsorption strength, is directly connected to the desorption temperature of the probe molecule from the catalyst surface.[40,41] The two upper files of Fig. S8 (panels a–d) show representative examples of such analysis for selected catalysts. The bottom panel (Fig. S8e) of this figure provides a comparison of the adsorption capability of the samples. A mild increase in basicity is observed in the presence of magnesium. Magnesium significantly decreases the acidity of the surface by decreasing the population of the medium-strength acid sites and increasing that of low-strength acid sites, which then become dominant.

2.2 Photocatalytic H_2 production

The functional properties of the systems were tested in the photocatalytic production of hydrogen. Production of hydrogen using methanol as a sacrificial molecule occurs through a mechanism where the alcohol adsorbed on anatase is attacked by hole-related species, producing simultaneously oxidized carbon-containing molecules and protons.[7,42,43] Molecular Hydrogen is formed through proton coupling occurring at the platinum cocatalyst. This requires the concomitant consumption of electrons.[42,43] At a fixed temperature (room temperature), the kinetics of the photoproduction of hydrogen are a function of three main variables, the catalyst concentration, the methanol : water ratio, and the illumination intensity.[42–44] The response of our catalysts was analyzed using a Box–Behnken factorial design.[45] Fig. 3 displays the results of this study for the PtT and Pt3.75Mg samples, while Fig. S9 shows the results for the Pt5Mg catalyst. To study the response to the abovementioned variables, Pareto plots (Fig. S10) were utilized to visualize the catalytic response of the solids, which was modelled using linear, quadratic and crossed terms between the three factors.[46] Pareto charts of standardized effects provide graphical evidence of the statistically significant parameters, that is, those that are above the established threshold. For a parameter to be statistically significant, the null hypothesis of the parameter coefficient being equal to zero is tested by comparing the calculated ANOVA p-value with a significance test level here set at α = 0.05 (95% probability). If the p-value is less than α, the hypothesis that the coefficient is equal to zero is rejected, and it is deemed to be statistically significant. In Fig. S10, the length of the plotted bars is a graphical representation of the weight of the parameters.

The Pareto plots provide evidence of the profound effect of magnesium on photocatalytic behavior (Fig. S10). The response of the PtT sample is essentially sensitive to irradiation in the ranges studied (Fig. 3). The irradiation level triggers a response with a rough power dependence of 0.5 of the intensity at the reactor ($I_{\lambda,\Omega}$ measured as described in the SI section, eqn (2)). This behavior has been observed previously and was discussed in detail in kinetic studies of hydrogen photoproduction.[43] The optimum methanol : water ratio is close to a CH_3OH : H_2O 50 : 50 ratio for all samples. The response to different methanol : water mixtures was extensively studied previously, showing increasing behavior for methanol concentrations up to *ca.* 30% and steadier behavior for higher concentrations of alcohol. The optimum of 50 : 50 or methanol-rich mixtures is typical of platinum-promoted anatase systems.[20,47] For the catalyst concentration, the most important effect is the significantly lower quantity required to optimize the response in the presence of magnesium at the catalyst composition. The optimum catalyst concentration changes from 0.27 mg mL^{-1} for the PtT sample to 0.12 mg mL^{-1} for the Pt3.75Mg sample

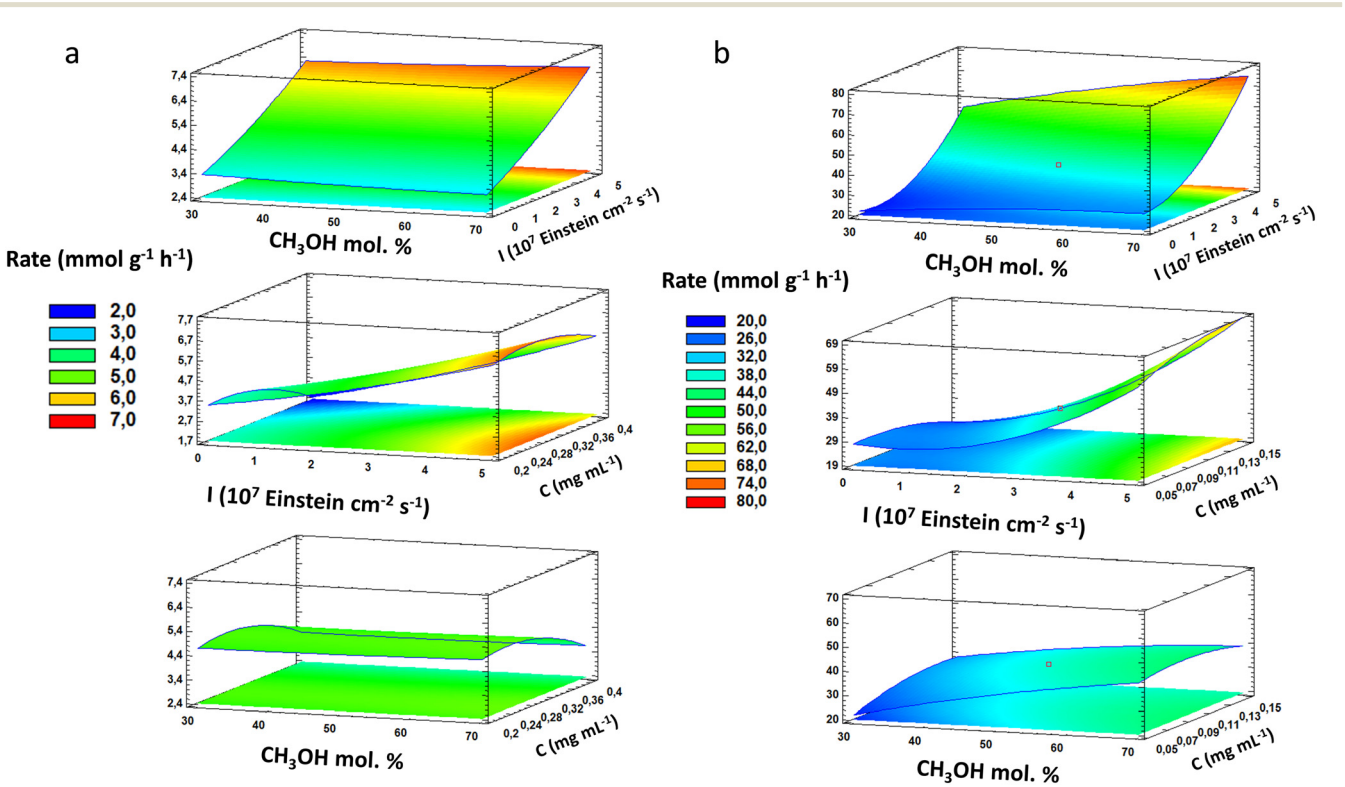

Fig. 3 Contour plots and basal projection of the modeled catalytic response obtained at the central point of (catalyst concentration, methanol mol% content of the liquid phase, and irradiation intensity at, respectively, top, middle, and lower positions of the columns), the three variables used in the experimental design (Table S1). Data for (a) PtT and (b) Pt3.75Mg samples are presented.

(Fig. 3). The minimum quantity of magnesium included in the catalyst formulation (Pt1Mg) has a strong effect, with an optimum concentration of 0.17 mg mL^{-1}. The result of the optimization is that magnesium is able to enhance the reaction rate by *ca.* 10.4 times (Pt3.75Mg *vs.* PtT). The strong catalytic effect of atom-dispersed magnesium entities is thus evident. The combined effect of platinum and magnesium can also be noted, taking into account that the 3.75Mg support presents rather low activity, nearly 23 times lower than that of the Pt3.75Mg sample. Meanwhile, carbon dioxide was the only gas-phase molecule detected along with hydrogen in the experiments. This was also observed in previous contributions.[8,18,48] The CO_2 production rates are presented in Table S4.

To further study the promotion effect of atom-dispersed magnesium, we analyzed the quantum efficiency parameter. Quantum efficiency describes the performance of the catalyst per unit photon (Einstein) absorbed by the powder under reaction conditions. It is the parameter that the IUPAC (International Union of Pure and Applied Chemistry)

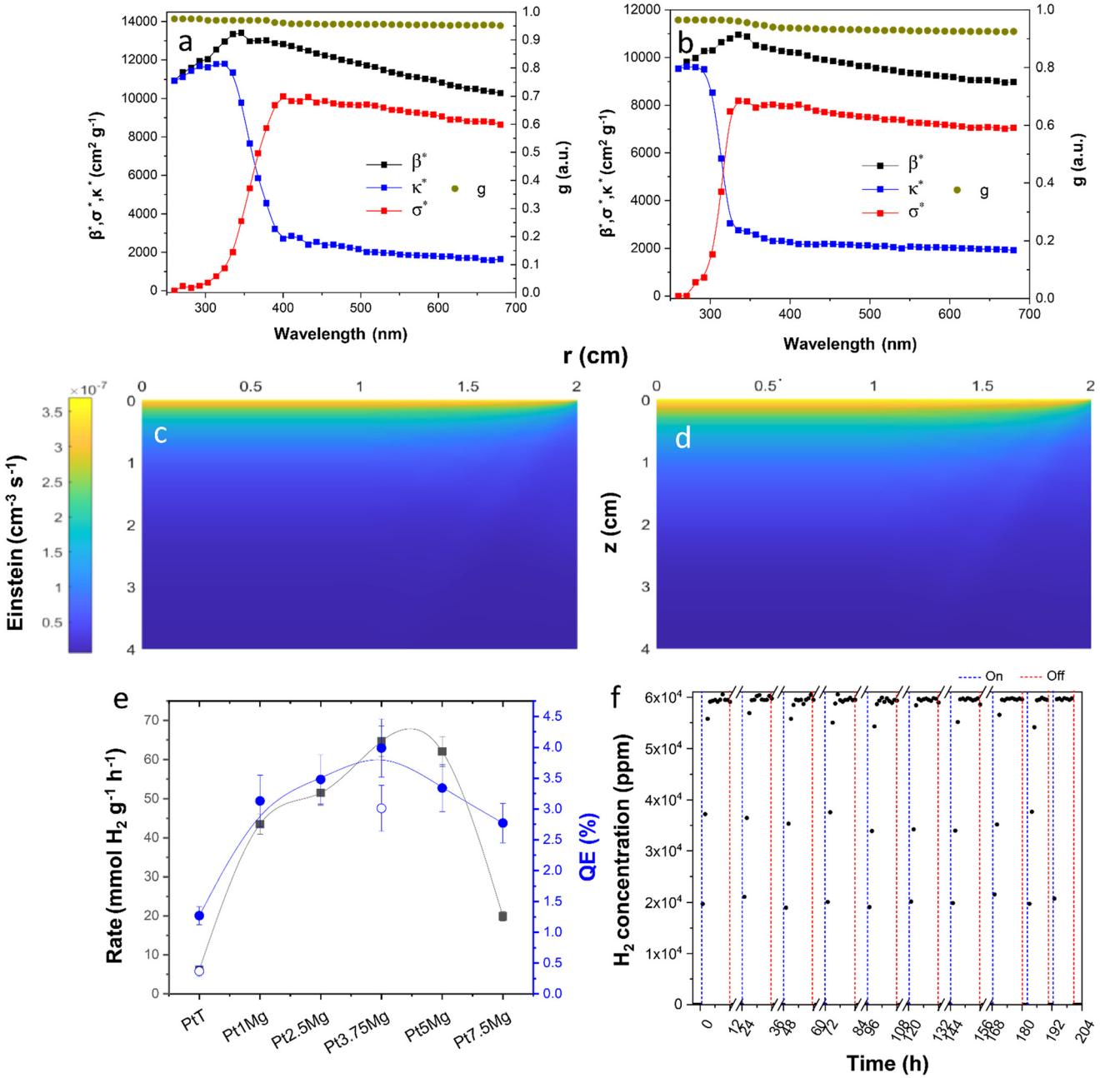

Fig. 4 Optical properties of the solid–liquid suspensions (a and b) and volumetric rate of photon absorption (c and d) for the PtT (a and c) and Pt3.75Mg (b and d) samples under optimum reaction conditions; (e) the reaction (squares) and quantum efficiency (closed circles, UV, open circles (sunlight)) for the samples; (f) a light-on/off cycling experiment for the Pt3.75Mg sample.

recommends to compare the activity of photocatalysts.[25,49] A comparison of the activity performance of our samples and benchmark materials is presented in Table S5.

To obtain quantum efficiency values, Fig. 4 displays the relevant optical properties of the catalyst suspension for values of the reaction medium (methanol-to-water ratio) and illumination conditions rendering optimum catalytic response (Fig. S11, Table S6). Note that this takes place with a single difference between the (reaction) operation variables, the optimum catalyst concentration around which the catalytic activity was studied (Table S6). The optical variables relevant for analyzing activity for a suspended catalyst (liquid phase) are described in eqn (1) and (2) (section 4.3). For representative samples, the spectral extinction coefficient (β_λ), spectral absorption coefficient (κ_λ), and the spectral scattering coefficient (σ_λ) are presented in Fig. 4a and b for the UV-visible range. The corresponding local volumetric rate of the photon absorption (E^a) parameter over the (z, r) plane of a (cylindrical) reactor volume is shown in Fig. 4c and d. The entire reactor volume is obtained by repeating this plane by rotation around the central axis of the reactor (Fig. S12b). The effect of magnesium on the relevant optical properties of the catalyst suspension becomes evident in the radial-averaged $E^{a,\nu}$ profiles displayed in Fig. S13. The step decrease in the PtT signal is likely a critical effect for optimizing the solid–light interaction under reaction conditions. As a result of the strong differences in optical properties and light intensity at the reactor, the response of the catalyst should be compared at optimum conditions for all samples, as previously indicated.[43]

The reaction rates and corresponding quantum efficiency values for the catalysts of the series under optimum conditions (maximizing the catalytic response) are presented in Fig. 4e. Both parameters show relatively similar behavior throughout the series of samples. The optimum activity seems to be located for a magnesium concentration of 3.75 to 5 mol%. As mentioned, a comparison with previously reported reaction rates of magnesium-promoted systems is shown in Table S5 (entries 1 and 2). Although previous work uses different reaction conditions, making a clear assessment difficult, the rates expressed per gram of catalyst are significantly lower than those presented here. One of the studies reported the photonic yield for single-line excitation (350 nm) but did not report the corresponding solar illumination (AM 1.5G).[24] Considering the information presented in the above mentioned contribution, it would be below 2%. Comparison with our best sample (Table S5; Pt3.75Mg), rendering a near *ca.* 50% higher quantum efficiency, provides evidence for the strong promotion effect of magnesium, as measured by both the reaction rate and the quantum efficiency. A general comparison with literature reports for titania-based catalysts is also presented in Table S5. Again, differences in measurement conditions do not make it easy to compare results. Nevertheless, reaction rates of our samples are among the highest (Table S5, entries 1–8). Comparison using the (true) quantum efficiency, the only parameter allowing quantitative analysis, can only be carried out with a very few systems, although it also favors our systems (Table S5, entries 7 and 8). Furthermore, we would like to stress the fact that, according to the quantum efficiency parameter, when using the Pt3.75Mg sample, the PtT reference activity is improved by 3.1/8.2 times under UV/sunlight (AM 1.5G). Moreover, using the TOF parameter (calculated with the dispersion values presented in Table S2), the Pt3.75Mg sample displays a value of 2790 h^{-1}, a multiple of *ca.* 10.6 times the value of the PtT reference.

2.3 Long-term stability and interpretation of activity

As a last catalytic test, Fig. 4f provides evidence of the stability of our best sample under long-term operating conditions. For an on/off test over a total of *ca.* 200 h, our system does not show any sign of activity decay. The high quantum efficiency and the stable response obtained by promoting the PtT system with single-atom magnesium entities make this technology one of the most promising for a future in which hydrogen can be obtained from renewable sources. The stable catalytic response is closely connected to the physicochemical stability of the materials. Table S3 includes measurements of the BET area, primary particle size of anatase from XRD, and band gap energy from UV-visible spectroscopy. No significant changes are detected for any of the abovementioned parameters and samples of the series. To analyze the platinum and magnesium components of the most active Pt3.75Mg sample, we utilized XPS. Fig. 5a and b display the Pt 4d and Mg 1s XPs peaks and compare pre- and post-reaction (used) spectra of the Pt3.75Mg catalyst, the most active sample. The fitting of the corresponding spectra indicates only minor changes in the metallic Pt(0) nanoparticles and the atom-dispersed magnesium entities. The absence of any significant loss of platinum or magnesium from the surface is further corroborated by the results of chemical analysis included in Table S2. Furthermore, XPS shows the limited effect on dispersion of these two components (Fig. 5a and b), a conclusion reinforced by the microscopic study presented in Fig. S14. Moreover, Fig. S14 proves the stability of the single-atom magnesium entities under reaction conditions.

The results presented in the previous subsection (2.2) were able to show the similar electronic properties of the solids. Analysis of the optoelectronic properties (photoluminescence spectra, Fig. 2d, and photoresponse results, Fig. S4) provides evidence that charge carrier effects do not determine or control optimization of the photoactivity in our samples. In particular, rather similar structural/electronic properties were observed for samples with a magnesium molar content between 1 and 5%. Despite the positive role played by Mg in decreasing charge recombination and increasing electron transport capability under illumination, no obvious correlation is observed between catalytic performance (quantum efficiency; Fig. 4e) and photoluminescence/photoresponse intensity (Fig. 2d and S4) throughout the

series of samples. In parallel, the surface properties of the solids were analyzed using TPD and two probe molecules (CO_2 and NH_3). This study shows that the presence of magnesium alters the acidity of the surface (Fig. S8d).

To interpret the effects of magnesium on activity triggered by the modification of the surface properties, we carried out *in situ* infrared experiments in the dark and under illumination conditions. Fig. 5c and d display results for the PtT and Mg3.75Mg samples, and Fig. S15a for the Pt5Mg sample. For the PtT reference, the adsorption of the reaction mixture in the dark shows a displacement of the water (negative band corresponding to the bending mode at *ca.* 1640 cm^{-1}) by carbon-containing species. These species generate only very weak and ill-defined bands. Under illumination, a broad and prominent band appears at *ca.* 1583 cm^{-1} with shoulders at *ca.* 1496 and (a rather weak one

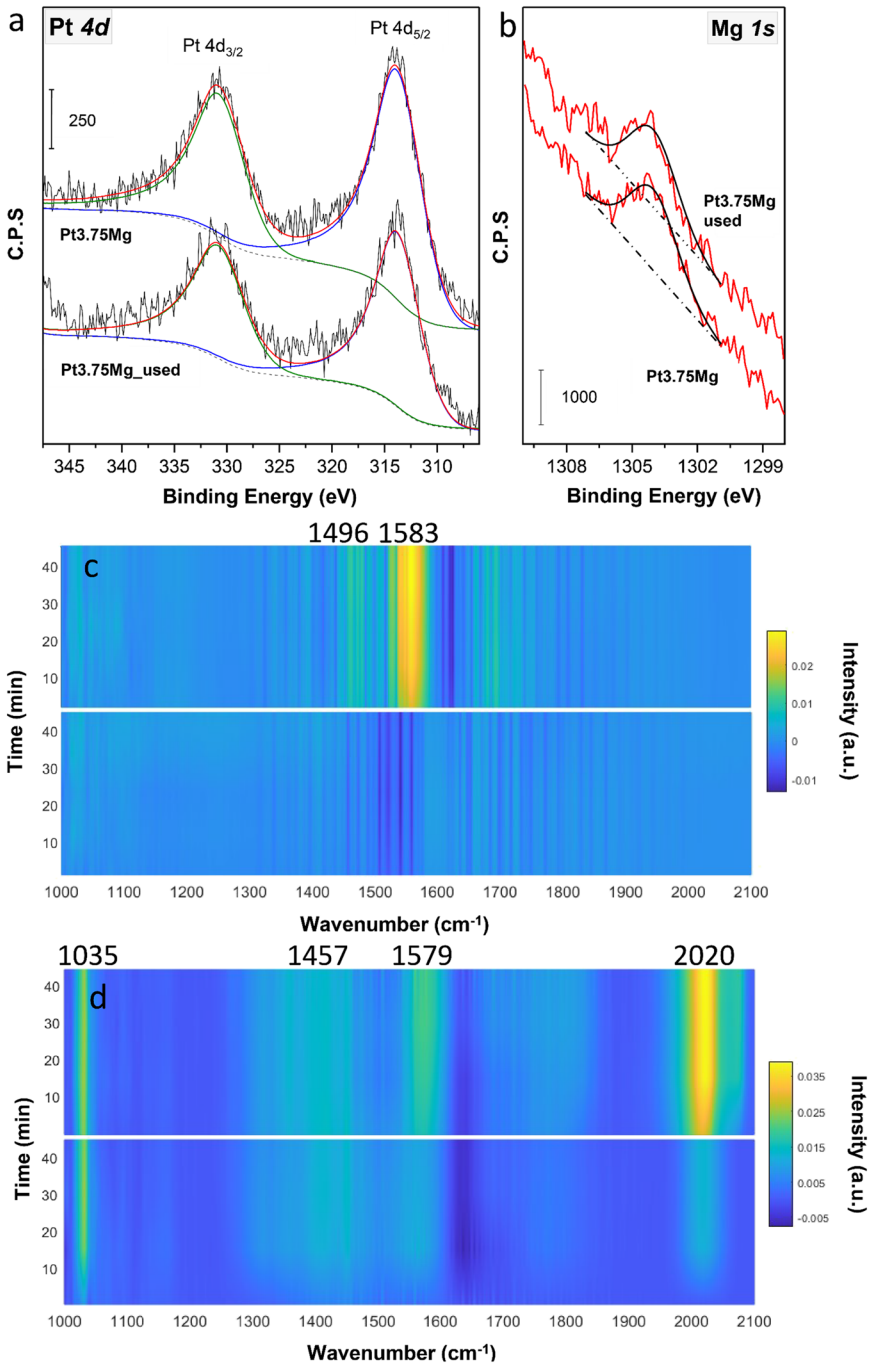

Fig. 5 XPS fitting and experimental results for pre- and post-reaction specimens of the Pt3.75Mg sample. (a) Pt 4d, and (b) Mg 1s signals; (c and d) *in situ* infrared spectra of the reaction mixture in the dark (bottom) and under illumination (top) conditions for the PtT (c) and Pt3.75Mg (d) catalysts.

at) 1685 cm^{-1} (Fig. 5c). These bands can be attributed to carbonates and carboxylates at the anatase surface.[18,50–52] Clear differences can be visualized when comparing the *in situ* infrared results of the PtT reference and two active single-atom-promoted magnesium samples (Pt3.75Mg, Fig. 5d, and Pt5Mg, Fig. S15a). Magnesium-promoted samples present several bands in the dark. A band at *ca.* 1035 cm^{-1} is observed and assigned to the C–O stretching of methoxy species.[50,53] A first difference thus comes directly from the promoted interaction with the sacrificial molecule, the alcohol (Fig. S15b). Other bands are observed at 1457–1458, 1568–1579, and 2020 cm^{-1}. The first two bands can be assigned to bridge formate species, and the last corresponds to carbonyl species adsorbed over Pt nanoparticles.[18,50–52] Differences between active samples would concern mainly the lower adsorption capability of methanol for the Pt5Mg sample (Fig. S15b), but the higher capability of formation of bridge formate species with respect to Pt3.75Mg (Fig. S15c). Similar behavior is observed for Pt*x*Mg (x = 3.75, 5) in the C═O stretching region (2020 cm^{-1}; Fig. S15d), Pt5Mg showing higher surface coverage values for (carboxylate-type and) CO species.

The IR study demonstrates that the presence of atom-dispersed magnesium entities has a strong effect on the methanol coverage of the anatase surface but also plays a relevant role in the reaction mechanism and kinetics. The presence of magnesium favors the attack of the hole-related species ($h^{+}/OH^{\bullet}$) on the surface-adsorbed methanol molecule. This mainly occurs through a step-like mechanism with the potential formation of several (oxidized) carbon-containing intermediates, such as aldehyde-type, acid-type precursors and, finally, carbon oxide molecules.[54,55] In our case, it renders bridge-carboxylate as the main surface species ($CH_3OH + H_2O + 4\ h^{+} \rightarrow CHOOH + 4H^{+}$). Note that this generates protons from both the alcohol and water molecules. Although water can play a role (mainly through hydroxyl-type radical species) in all the above mentioned oxidation steps, the formation of carboxylate species appears as the first step (in the step-type oxidative mechanism of the alcohol), where water is consumed. Such consumption does not take place, for example, in the generation of aldehyde-type precursor species. In any case, carboxylate-type species and maybe other minor species appear to suffer decarbonylation-type reactions generating CO and more protons ($CHOOH \rightarrow CO + OH^{-} + H^{+}$).[18,42,48] Finally, in the case of the magnesium-containing active samples, CO at Pt surfaces is transformed through the reverse water-gas-shift reaction ($CO + H_2O \leftrightarrow H_2 + CO_2$).[18,50,52] The latter renders CO_2, the single carbon-containing molecule detected in the gas phase, as observed previously in other studies.[8,18,48] Note thus that the carboxylate-type species do open a reaction pathway out of the step-like mechanism. Evidence of the key role of the carbonyl intermediate to promote activity can be obtained from IR results using a physical mixture between the PtT sample and the 3.75Mg support (Fig. S16). The absence of the above mentioned carbonyl species can be noted, indicating that both magnesium and platinum components of the active Pt*x*Mg catalysts are required to rapidly produce the carboxylate species.

The radar plot presented in Fig. 6a summarizes the most relevant results to interpret activity on a physical basis, and Fig. 6b provides a schematic representation of such properties. After the previous discussion, Fig. 6a compares the activity of the samples with the acidity–basicity "strength" of the surface (as measured using TPD results), the surface concentration of methanol and CO (derived from IR results; note that carboxylates and CO species demonstrate rather similar behavior for each active Pt*x*Mg sample of the series;

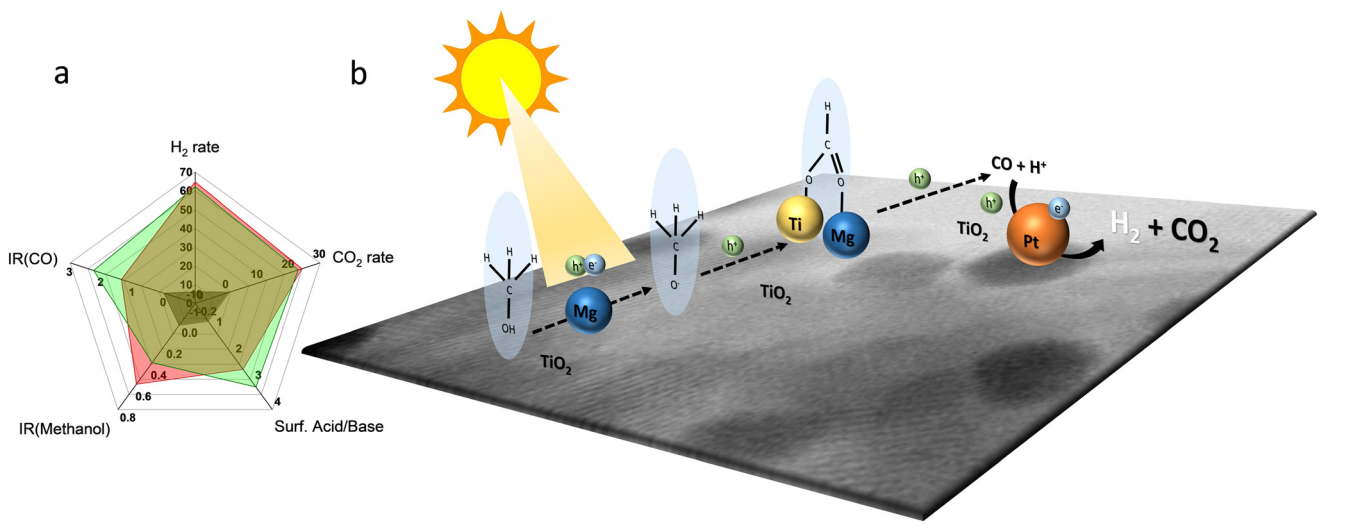

Fig. 6 (a) Radar plot displaying catalytic (H_2 and CO_2 reaction rates) and relevant physicochemical properties (surface acid/base, as measured by TPD; and absorbed quantity of methanol and CO under reaction) for selected samples. Black, PtT; red, Pt3.75Mg, green, Pt5Mg. See text for details. (b) Schematic representation of the catalytic role of the different components of the catalyst and their promotional effects taking place under illumination.

Fig. S15) as well as the CO_2 production rates. The magnesium promotion effect is maximized by the enhancement of: i) the adsorption capability of the surface for the sacrificial molecule, as a consequence of the decreased acidity of the surface, and ii) the subsequent reaction steps related to the hole attack on the molecule, decarbonylation and the water-gas-shift reaction. Comparison of the two best samples (Pt3.75Mg and Pt5Mg) would indicate that the population of the anatase surface by single-atom magnesium entities reaches an optimum (measured using the quantum efficiency parameter) for the Pt3.75Mg case, where the transformation of methanol to bridge carbonate is followed by quick evolution of this last surface species, leading to carbon monoxide (and dioxide) species (Fig. 6). Above that optimum (Pt3.75Mg), the Pt5Mg sample would show a decrease in the interaction with methanol, disfavoring its adsorption, and the transformation of the bridge-bonded carboxylate and CO species appears to be somewhat slower, facilitating the growth of their surface population (Fig. 6a). As previously mentioned, in all the above discussed steps, hydrogen ions are co-generated. At the cocatalyst (platinum) surface, these ions and electrons are efficiently combined to maximize the hydrogen yield (Fig. 6a and b). The role of platinum in such a step and the water-gas-shift reaction would be relatively similar in all active samples. This could be a consequence of the rather similar primary particle size and dispersion (Fig. 1, Table S2), and interaction with the magnesium-promoted support. Note that the facile decomposition of carboxylate species and the concomitant production of carbonyl-type species both require the participation of magnesium and platinum species at the surface of Pt*x*Mg samples. This is schematically shown in Fig. 6b. The mechanism of the interaction between platinum and magnesium is likely to involve effects on the surface diffusion of intermediate species. In any case, Fig. S16 shows the infrared results for a physical mixture between the PtT reference and the 3.75Mg support. The species detected, as well as their evolution under reaction, display strong similarities (obviously, the signal is weaker) with the PtT reference sample, where the carboxylate-type species appear to show restricted evolution, limiting activity.

3 Conclusions

A significant enhancement in the hydrogen production by the Pt–TiO_2 system is achieved here using magnesium, a cheap and widely available promoter. To prove it, we synthesized materials using a microemulsion method, which ensures the maximum interaction and dispersion of magnesium at the main component (titania) surface. A series of catalysts with magnesium content from 0.5 to 7.5 mol% was prepared. The resulting catalysts correspond to high-surface-area mesoporous materials with anatase as the dominant phase. They present BET surface area and band gap energy with relatively minor changes between the samples of the series, and an essentially invariant primary particle size for the Pt component. The promoter is present predominantly as Mg(II) species atomically dispersed onto the anatase surface.

A content of Mg between 3.75 and 5 mol% optimizes activity and triggers stability under long-term operating conditions. The promoting effect is here measured using a full experimental design (methanol-to-water, catalyst concentration, and illumination intensity) and comparing the reaction rates and, more importantly, the quantum efficiency values rendered by the samples. The photocatalytic activity, expressed in terms of quantum efficiency, increased 8.2-fold relative to the Pt–TiO_2 reference under sunlight. This appears to be the maximum value achieved so far, to the best of our knowledge, using magnesium as a promoter. The presence of atom-dispersed magnesium species favored the control over charge carrier recombination and handling, yet the photoluminescence and photoresponse experiments showed limited influence on maximizing the activity. In contrast, the *in situ* infrared experiments rationalize the promotion of catalytic activity. The atom-dispersed promotion has a significant influence on both the adsorption of the sacrificial molecule as well as its evolution on the anatase surface to generate bridge formate species *via* hole attack. This carbon-containing species appears to decarbonylate and generate CO, which, in turn, is transformed with the help of the platinum co-catalysts through the water-gas-shift reaction. As a result, a cheap and widely available single-atom magnesium promoter appears to be an economically and environmentally respectful way to obtain hydrogen from renewable energy and bio-based carbon-based sources.

4 Experimental section

4.1 Catalyst preparation

To maximize magnesium interaction with the titania support, we utilized a microemulsion method. To start the synthesis, an inverse (water-in-oil) microemulsion using *n*-heptane (aqueous phase dispersing agent; Sigma-Aldrich), Triton X-100 (surfactant; Sigma-Aldrich) and hexanol (cosurfactant; Sigma-Aldrich) was prepared. After stirring the mixture for *ca.* 30 min, certain quantities of magnesium (magnesium nitrite precursor; Sigma-Aldrich) were added as described below. After a few minutes, titanium tetraisopropoxide diluted in isopropanol (2 : 3) was added dropwise to the final microemulsion. The microemulsion utilized water/(Ti + Mg) and water/surfactant molar ratios of 18 and 110, respectively. The hydrolysis of the titania precursor initially produces molecular entities with unbalanced electrostatic charge, enabling their easy interaction with magnesium ions.[18] After overnight stirring, the suspension was centrifuged, decanted, rinsed (methanol and Milli-Q water), and dried in a furnace at 100 °C overnight. Finally, the powders were thermally treated at 450 °C for 2 h.

The platinum cocatalyst (1 wt% with respect to the support) was introduced in the catalyst composition using a chemical deposition method. An H_2PtCl_6 (Sigma-Aldrich)

compound was utilized as a precursor. In the first step, the calcined support was introduced into the water and sonicated for 30 min under a nitrogen atmosphere. The platinum precursor was then added to the suspension. Finally, the $NaBH_4$ was used as a reducing agent to convert the noble metal to its zero-valent state. The Pt : $NaBH_4$ molar ratio utilized was 1 : 5.[18] The resulting suspension was sonicated for 15 minutes, and the resulting solid was recovered by centrifugation, washed several times with deionized water, and finally dried overnight at 80 °C. The synthesized powders were labeled Pt/*x*Mg, where *x* indicates the molar amount of magnesium with respect to the Ti cation present in each solid. Thus, *x* was essayed from 0.5 (0.5 : 99.5Mg : Ti) to 7.5 (7.5 : 92.5Mg : Ti). A Pt–titania (PtT) reference system was also synthesized.

4.2 Catalyst characterization

Elemental analysis was determined using inductively coupled plasma atomic absorption spectroscopy (ICP-OES) (PerkinElmer Optima 3300 DV). A Panalytical-Aeris diffractometer, using monochromatic CuKα radiation (λ = 0.154056 nm), was utilized to obtain the XRD patterns. UV-vis testing (catalyst powders) was carried out using a Cary-5000 (Agilent Technologies) UV-vis near infrared spectrometer and an integrating sphere in the 800–200 nm range. The Kubelka–Munk correction was applied to all spectra. Band gap analysis was carried out by plotting $(h\nu a)^{1/2}$ ($h\nu$ = excitation energy, a = absorption coefficient, proportional to the Kubelka–Munk transformation) as a function of the excitation energy. This considers that anatase is an indirect gap semiconductor. A fluorescence spectrophotometer (Horiba FluoroMax Plus, Germany) was utilized to obtain photoluminescence spectra of the solids as films and normalized by the adsorption at the excitation wavelength (365 nm). The photoelectrochemical experiments were performed using the same films, and an Autolab PGSTAT320 N potentiostat/galvanostat controlled by NOVA 2.1 software. FTO pieces (2.5 cm × 2.5 cm, 5.29 cm^2) were coated with the studied photocatalysts. A 500 W Xe lamp was used as a radiation source (Quantum Design). The measurements were performed in a quartz reactor, using the photocatalysts as working electrodes, Ag/AgCl (3 M) as reference electrode and Pt wire as counter electrode. The electrolyte (pH 7.3) was a 0.1 M Na_2SO_4 (Sigma-Aldrich, ACS reagent, >99%) solution. During the photoelectrochemical characterization, the photoelectrode was irradiated on the reverse side and facing the counter electrode. Linear sweep voltammetry (LSV) experiments were carried out from +1 V Ag/AgCl to −0.6 V *vs.* Ag/AgCl with a scan rate of 5 mV s^{-1}, chopping irradiation with an on/off frequency of 20 s. A TRISTAR II instrument (Micromeritics) was used to measure nitrogen adsorption–desorption isotherms and to determine the BET surface area and textural properties of the materials. X-ray photoelectron spectra (XPS) of the solids were recorded using a SPECS® spectrometer (UK) with a PHOIBOS® 150 WAL hemispherical energy analyzer with angular resolution (<0.5°), equipped with XR 50 X-ray Mg and Al-X-ray and μ-FOCUS 500 X-ray monochromator (Mg, Al excitation line) sources. To account for charging effects, the binding energies (BE) were referenced to the C 1s peak (284.6 eV). High-resolution transmission electron (HR-TEM) and scanning transmission electron (HR-STEM) microscopy were utilized to interrogate the solids and study their morphology and structure using a JEOL 2100F TEM/STEM microscope (Japan). The apparatus is equipped with an energy dispersive X-ray spectrometer (EDS) to measure chemical composition.

Diffuse reflectance infrared spectroscopy (DRIFTS) was utilized to measure the catalyst response to the reaction environment. The apparatus is a Bruker Vertex 80 FTIR spectrometer using an MCT detector and running under OPUS/IR software. A water-to-methanol mixture (optimum of the factorial design described in section 2.2) was injected into an Ar stream (10 mL min^{-1}) and contacted with the catalyst in a reaction cell (HVC, Harrick Scientific) located in a praying mantis DRIFTS accessory (Harrick Scientific). The illumination source is the same as that used in the reaction experiments (see below). The DRIFT signal was accumulated for *ca.* 1.5 s for a total of 10 scans over the 4000–600 cm^{-1} range. The background is taken before the reaction mixture enters the reaction chamber. Contact with the reaction mixture takes place under dark conditions and is continuously scanned until stability of the IR signal of the absorbed species is achieved. After the light is switched on, the IR signal is also monitored until stability is reached.

Thermo-programmed desorption experiments were carried out using a U-shaped home-made reactor coupled with a thermal conductivity detector (TCD). CO_2 and NH_3 molecules were used to analyze surface basicity and acidity, respectively. Samples were subjected to a stream of the corresponding gas at 50 °C, subsequently subjected to a purge with nitrogen until a stable TCD signal was achieved and then subjected to a temperature ramp at a rate of 10 °C min^{-1}.

4.3 Activity measurements

The functional properties of the materials were tested in a semi-continuous reactor (see the liquid phase reactor section in the electronic SI). A suspension of the catalyst (tested from 0.05 to 1 g L^{-1}) in a mixture of methanol : water (tested from 30 : 70 to 70 : 30 v/v) was used to produce hydrogen gas. The reactor has a volume of 80 mL, and the suspension occupies 40 mL. The hydrogen gas was evacuated continuously from the reaction using an Ar stream (10 mL min^{-1}). The Ar stream was stabilized under dark conditions.

Two experiments, under UV (280–400 nm) and visible (400–680 nm) light, were carried out using an Xe 500 W arc lamp coupled with dichroic and IR filters (Quantum LOT). The optimal reaction conditions to carry out the reaction were analyzed using a Box–Behnken factorial design (Table S5). The gas–liquid reactor and experimental procedures to optimize the catalyst concentration, methanol : water, and the

illumination intensity ratio are described in the SI section and are based on previous work.[7,18] Hydrogen production was obtained in continuous mode (Fig. S1) and measured using mass spectrometry (Omnistar 200; Pfeiffer). Values for the hydrogen production rate and the quantum efficiency parameters were obtained following IUPAC-recommended procedures.[25] Eqn (1) shows the calculation of the quantum efficiency. It utilizes the reaction rate (r) and the local volumetric rate of photon absorption (E^{a}). Both parameters correspond to average values (subscript A) obtained over the entire volume of the reactor.

$$\mathrm{QE}\,(\%) = \frac{\langle r\rangle_A}{\langle E^{a}\rangle_A} \times 100 \tag{1}$$

To calculate the E^{a} parameter, the optical properties of the suspension and the modeling of the light–catalyst interaction at the reactor were carried out, as described in the SI section. As a first step to calculate the quantum efficiency (eqn (1); Fig. S10 and S11), we measured the spectral absorption, κ_λ, and the spectral scattering, σ_λ, coefficients. The Henyey–Greenstein equation provides an analytical formula for the scattering phase ($p(\underline{\Omega}' \rightarrow \underline{\Omega})$). With this information, the radiative transfer equation (RTE) (eqn (2)) was solved in our reactor.

$$\frac{\mathrm{d}I_{\lambda,\underline{\Omega}}(\underline{x})}{\mathrm{d}s} = -\kappa_\lambda I_{\lambda,\underline{\Omega}}(\underline{x}) - \sigma_\lambda I_{\lambda,\underline{\Omega}}(\underline{x}) + \frac{\sigma_\lambda}{4\pi}\int_{\Omega'=4\pi} p(\underline{\Omega}' \rightarrow \underline{\Omega}) I_{\lambda,\underline{\Omega}'}\mathrm{d}\underline{\Omega}' \tag{2}$$

Eqn (2) is, in fact, solved through a recursive procedure using the discrete ordinate method to obtain a numerical solution. As a boundary condition to solve the integro-differential eqn (2), the light intensity at the illuminated surface of the reaction was measured using actinometry (Fig. S10), and then the intensity of light throughout the reactor volume ($I_{\lambda,\underline{\Omega}}(\underline{x})$) was calculated. Finally, the E^{a} parameter can be obtained: $E^{a} = \int_\lambda \kappa_\lambda(\underline{x}) \cdot \int_{\Omega=4\pi} I_{\lambda,\underline{\Omega}}(\underline{x})\mathrm{d}\Omega\mathrm{d}\lambda$. Full details of the calculation of the parameters described in this subsection can be found in previous work and are summarized in the SI (section Liquid Phase Reactor: Local volumetric rate of photon absorption calculation).[7,18,49]

Author contributions

Esperanza Fernández-García, data curation; formal analysis; validation; visualization; writing – original draft. Uriel Caudillo-Flores, data curation; formal analysis; funding acquisition; investigation; methodology; project administration; resources; validation; visualization; writing – review & editing. Rocío Sayago-Carro, data curation; formal analysis; validation; visualization; writing – review & editing. A. Tolosana-Moranchel, data curation; formal analysis; investigation; visualization. Marcos Fernández-García, conceptualization; data curation; formal analysis; funding acquisition; investigation; methodology; project administration; resources; software; supervision; validation; visualization; writing – original draft; writing – review & editing. Anna Kubacka, conceptualization; data curation; formal analysis; funding acquisition; investigation; methodology; project administration; resources; software; supervision; validation; visualization; writing – original draft; writing – review & editing.

Conflicts of interest

The authors declare no conflict of interest.

Data availability

The data of this article have been included in this published article and its supplementary information (SI). Further information and data will be made available upon request.

Supplementary information is available. See DOI: https://doi.org/10.1039/d5im00219b.

Acknowledgements

Financial support for this work was obtained through the IA104422 PAPIIT-UNAM (Mexico) project and through grants PID2022-136883OB-C21, CETP-FP-2023-00250, and PCI2024-155031-2 funded by MCIN/AEI/https://doi.org/10.13039/501100011033 and, when appropriate, by the "European Union" EU/PRTR and FEDER/EU programs. Mr. D. A. Dominguez and Mr. F. Ruiz are acknowledged for the XPS spectra and TEM images, respectively. M. F. G. is fully indebted to Prof. F. Fernández-Martín for its support and guide.

References

1 A. Kubacka, M. Fernández-García and G. Colón, Advanced nanoarchitectures for solar photocatalytic applications, *Chem. Rev.*, 2012, **112**, 1555–1614.
2 Y. Zhao, Y. Li and L. Sun, Recent advances in photocatalytic decomposition of water and pollutants for sustainable application, *Chemosphere*, 2021, **276**, 130201.
3 L. Chang, S.-T. Yong, S.-P. Chai, L. K. Putri, L.-L. Tan and A. R. Mohamed, A review of methanol photoreforming: Elucidating the mechanisms, photocatalysts and recent advancement strategies, *Mater. Today Chem.*, 2023, **27**, 101334.
4 E. C. Okonkwo, M. Al-Breiki, Y. Bicer and T. Al-Ansari, Sustainable hydrogen roadmap: A holistic review and decision-making methodology for production, utilisation and exportation using Qatar as a case study, *Int. J. Hydrogen Energy*, 2021, **46**, 35525–35549.
5 M. Ismael, A review and recent advances in solar-to-hydrogen energy conversion based on photocatalytic water splitting over doped-TiO_2 nanoparticles, *Sol. Energy*, 2020, **211**, 522–546.
6 A. Kubacka, U. Caudillo-Flores, I. Barba-Nieto and M. Fernández-García, Towards full-spectrum photocatalysis: Successful approaches and materials, *Appl. Catal., A*, 2021, **610**, 117966.
7 U. Caudillo-Flores, M. J. Muñoz-Batista, M. Fernández-García and A. Kubacka, Bimetallic Pt-Pd co-catalyst Nb-doped TiO_2

materials for H_2 photo-production under UV and Visible light illumination, *Appl. Catal., B*, 2018, **238**, 533–545.

8 A. López-Martín, F. Platero, A. Caballero and G. Colón, Thermo-photocatalytic methanol reforming for hydrogen production over a CuPd–TiO_2 catalyst, *ChemPhotoChem*, 2020, **4**, 630–637.

9 V. Kumaravel, S. Mathew, J. Bartlett and S. C. Pillai, Photocatalytic hydrogen production using metal doped TiO_2: A review of recent advances, *Appl. Catal., B*, 2019, **244**, 1021–1064.

10 M. Ni, M. K. H. Leung, D. Y. C. Leung and K. Sumathy, A review and recent developments in photocatalytic water-splitting using TiO_2 for hydrogen production, *Renewable Sustainable Energy Rev.*, 2007, **11**, 401–425.

11 A. Kubacka, G. Colón and M. Fernández-García, Cationic (V, Mo, Nb, W) doping of TiO_2-anatase: A real alternative for visible light-driven photocatalysts, *Catal. Today*, 2009, **143**, 286–292.

12 J. C. Colmenares and R. Luque, Heterogeneous photocatalytic nanomaterials: Prospects and challenges in selective transformations of biomass-derived compounds, *Chem. Soc. Rev.*, 2014, **43**, 765–778.

13 A. Meng, L. Zhang, B. Cheng and J. Yu, Dual cocatalysts in TiO_2 photocatalysis, *Adv. Mater.*, 2019, 1807660.

14 C. Xia, T. Hong Chuong Nguyen, X. Cuong Nguyen, S. Young Kim, D. L. T. Nguyen, P. Raizada, P. Singh, V.-H. Nguyen, C. Chien Nguyen, V. Chinh Hoang and Q. Van Le, Emerging cocatalysts in TiO_2-based photocatalysts for light-driven catalytic hydrogen evolution: Progress and perspectives, *Fuel*, 2022, **307**, 121745.

15 P. Jimenéz-Calvo, M. J. Muñoz-Batista, M. Isaacs, V. Ramnarain, D. Ihiawakrim, X. Li, M. Ángel Muñoz-Márquez, G. Teobaldi, M. Kociak and E. Paineau, A compact photoreactor for automated H_2 photoproduction: Revisiting the (Pd, Pt, Au)/TiO_2 (P25) Schottky junctions, *Chem. Eng. J.*, 2023, **459**, 141514.

16 P. García-Muñoz, J. Ivanez, V. A. de la Peña O'Shea, N. Keller and F. Fresno, Solar hydrogen production from ethanol-water vapours over metal/TiO_2 photocatalysts supported on β-SiC alveolar foams, *Catal. Today*, 2023, **413–415**, 113987.

17 D. Wang, Z.-P. Liu and W.-M. Yang, Revealing the size effect of platinum cocatalyst for photocatalytic hydrogen evolution on TiO_2 support: A DFT study, *ACS Catal.*, 2018, **8**, 7270–7278.

18 O. Fontelles-Carceller, M. J. Muñoz-Batista, E. Rodríguez-Castellón, J. C. Conesa, M. Fernández-García and A. Kubacka, Measuring and interpreting quantum efficiency for hydrogen photo-production using Pt-titania catalysts, *J. Catal.*, 2017, **347**, 157–169.

19 M. Eder, C. Courtois, P. Petzoldt, S. Mackewicz, M. Tschurl and U. Heiz, Size and coverage effects of Ni and Pt Co-catalysts in the photocatalytic hydrogen evolution from methanol on TiO_2 (110), *ACS Catal.*, 2022, **12**, 9579–9588.

20 V. Kumaravel, M. Imam, A. Badreldin, R. Chava, J. Do, M. Kang and A. Abdel-Wahab, Photocatalytic hydrogen production: Role of sacrificial reagents on the activity of oxide, carbon, and sulfide catalysts, *Catalysts*, 2019, **9**, 276.

21 Z. Han, Y. Zhao, G. Gao, W. Zhang, Y. Qu, H. Zhu, P. Zhu and G. Wang, Erbium single atom composite photocatalysts for reduction of CO_2 under visible light: CO_2 molecular activation and 4f levels as an electron transport bridge, *Small*, 2021, **17**, 2102089.

22 Z. Sun, S. Cheng, X. Jing, K. Liu, Y. Chen, A. A. Wibowo, H. Yin, M. Usman, D. MacDonald, S. Cheong, R. F. Webster, L. Gloag, N. Cox, R. D. Tilley and Z. Yin, Atomic dispersed Co on NC@Cu core-shells for solar seawater splitting, *Adv. Mater.*, 2024, **36**, 2406088.

23 M. Fazil, S. M. Alshehri, Y. Mao and T. Ahmad, Hydrothermally derived Mg-doped TiO_2 nanostructures for enhanced H_2 evolution using photo- and electro-catalytic water splitting, *Catalysts*, 2023, **13**, 893.

24 L. Gao, Y. Li, J. Ren, S. Wang, R. Wang, G. Fu and Y. Hu, Passivation of defect states in anatase TiO_2 hollow spheres with Mg doping: Realizing efficient photocatalytic overall water splitting, *Appl. Catal., B*, 2017, **202**, 127–133.

25 S. E. Braslavsky, A. M. Braun, A. E. Cassano, A. V. Emeline, M. I. Litter, L. Palmisano, V. N. Parmon and N. Serpone, Glossary of terms used in photocatalysis and radiation catalysis (IUPAC recommendations 2011), *Pure Appl. Chem.*, 2011, **83**, 931–1014.

26 H. Zhang and J. F. Banfield, Understanding polymorphic phase transformation behavior during growth of nanocrystalline aggregates: Insights from TiO_2, *J. Phys. Chem. B*, 2000, **104**, 3481–3487.

27 M. Thommes, K. Kaneko, A. V. Neimark, J. P. Olivier, F. Rodriguez-Reinoso, J. Rouquerol and K. S. W. Sing, Physisorption of gases, with special reference to the evaluation of surface area and pore size distribution (IUPAC Technical Report), *Pure Appl. Chem.*, 2015, **87**, 1051–1069.

28 K. Madhusudan Reddy, S. V. Manorama and A. Ramachandra Reddy, Bandgap studies on anatase titanium dioxide nanoparticles, *Mater. Chem. Phys.*, 2003, **78**, 239–245.

29 L. Kong, C. Wang, H. Zheng, X. Zhang and Y. Liu, Defect-induced yellow color in Nb-doped TiO_2 and its impact on visible-light photocatalysis, *J. Phys. Chem. C*, 2015, **119**, 16623–16632.

30 C. C. Mercado, Z. Seeley, A. Bandyopadhyay, Z. Bose and J. L. McHale, Photoluminescence of dense nanocrystalline titanium dioxide thin films: Effect of doping and thickness and relation to gas sensing, *ACS Appl. Mater. Interfaces*, 2011, **3**, 2281–2288.

31 L. Kernazhitsky, V. Shymanovska, T. Gavrilko, V. Naumov, L. Fedorenko, V. Kshnyakin and J. Baran, Room temperature photoluminescence of anatase and rutile TiO_2 powders, *J. Lumin.*, 2014, **146**, 199–204.

32 F. Urbach, The long-wavelength edge of photographic sensitivity and of the electronic absorption of solids, *Phys. Rev.*, 1953, **92**, 1324–1324.

33 R. Favre, P. Raybaud and T. Le Bahers, Electronic structures of the MoS_2/TiO_2 (anatase) heterojunction: influence of

physical and chemical modifications at the 2D- or 1D-interfaces, *Phys. Chem. Chem. Phys.*, 2022, **24**, 2646–2655.
34 J. Yang, C. Li and P. Diao, Molybdenum doped $CuWO_4$ nanoflake array films as an efficient photoanode for solar water splitting, *Electrochim. Acta*, 2019, **308**, 195–205.
35 X. Lv, F. L.-Y. Lam and X. Hu, Developing $SrTiO_3/TiO_2$ heterostructure nanotube array for photocatalytic fuel cells with improved efficiency and elucidating the effects of organic substrates, *Chem. Eng. J.*, 2022, **427**, 131602.
36 P. E. Moulder, J. F. Stickle and W. F. Sobol, *Handbook of X-ray Photoelectron Spectroscopy: A Reference Book of Standard Data for Use in X-ray Photoelectron Spectroscopy*, Perkin-Elmer, 1993.
37 C. D. Easton and D. J. Morgan, Critical examination of the use of x-ray photoelectron spectroscopy (XPS) O 1s to characterize oxygen vacancies in catalytic materials and beyond, *J. Vac. Sci. Technol., A*, 2025, **43**, 053205.
38 H. Issa Hamoud, L. Wolski, I. Pankin, M. A. Bañares, M. Daturi and M. El-Roz, In situ and operando spectroscopies in photocatalysis: Powerful techniques for a better understanding of the performance and the reaction mechanism, *Top. Curr. Chem.*, 2022, **380**, 37.
39 M.-J. Choi, H. Park, M. H. Engelhard, D. Li, P. V. Sushko and Y. Du, Reevaluation of XPS Pt 4f peak fitting: Ti 3s plasmon peak interference and Pt metallic peak asymmetry in $Pt@TiO_2$ system, *J. Vac. Sci. Technol., A*, 2024, **42**, 063209.
40 N. Katada and M. Niwa, Analysis of acidic properties of zeolitic and non-zeolitic solid acid catalysts using temperature-programmed desorption of ammonia, *Catal. Surv. Asia*, 2004, **8**, 161–170.
41 M. Hu, Z. Yao and X. Wang, Characterization techniques for graphene-based materials in catalysis, *AIMS Mater. Sci.*, 2017, **4**, 755–788.
42 G. L. Chiarello, M. H. Aguirre and E. Selli, Hydrogen production by photocatalytic steam reforming of methanol on noble metal-modified TiO_2, *J. Catal.*, 2010, **273**, 182–190.
43 M. J. Muñoz-Batista, M. M. Ballari, A. Kubacka, O. M. Alfano and M. Fernández-García, Braiding kinetics and spectroscopy in photo-catalysis: The spectro-kinetic approach, *Chem. Soc. Rev.*, 2019, **48**, 637–682.
44 H. Liang, M. A. Rehan, J. Li, S. Du, Y. Zhai and G. Li, Kinetic simulation of hydrogen production reaction parameters based on TiO_2 photocatalyst, *Appl. Therm. Eng.*, 2024, **239**, 122134.
45 G. E. P. Box and D. W. Behnken, Some new three level designs for the study of quantitative variables, *Technometrics*, 1960, **2**, 455–475.
46 R. W. Mee, in *A Comprehensive Guide to Factorial Two-Level Experimentation*, John Wiley & Sons, 2009, pp. 397–414.
47 G. L. Chiarello, D. Ferri and E. Selli, Effect of the CH_3OH/H_2O ratio on the mechanism of the gas-phase photocatalytic reforming of methanol on noble metal-modified TiO_2, *J. Catal.*, 2011, **280**, 168–177.
48 R. Sayago-Carro, L. J. Jiménez-Chavarriga, E. Fernández-García, A. Kubacka and M. Fernández-García, Efficiency in photocatalytic production of hydrogen: Energetic and sustainability implications, *Energy Adv.*, 2024, **3**, 2738–2757.
49 U. Caudillo-Flores, M. J. Muñoz-Batista, M. Fernández-García and A. Kubacka, Recent progress in the quantitative assessment and interpretation of photoactivity, *Catal. Rev.: Sci. Eng.*, 2024, **66**, 531–585.
50 G. Halasi, G. Schubert and F. Solymosi, Comparative study on the photocatalytic decomposition of methanol on TiO_2 modified by N and promoted by metals, *J. Catal.*, 2012, **294**, 199–206.
51 X. Zheng, G. Zhang, Z. Yao, Y. Zheng, L. Shen, F. Liu, Y. Cao, S. Liang, Y. Xiao and L. Jiang, Engineering of crystal phase over porous MnO_2 with 3D morphology for highly efficient elimination of H_2S, *J. Hazard. Mater.*, 2021, **411**, 125180.
52 C. A. Walenta, C. Courtois, S. L. Kollmannsberger, M. Eder, M. Tschurl and U. Heiz, Surface species in photocatalytic methanol reforming on Pt/TiO_2 (110): Learning from surface science experiments for catalytically relevant conditions, *ACS Catal.*, 2020, **10**, 4080–4091.
53 A. Yamakata, T. Ishibashi and H. Onishi, Electron- and hole-capture reactions on Pt/TiO_2 photocatalyst exposed to methanol vapor studied with time-resolved infrared absorption spectroscopy, *J. Phys. Chem. B*, 2002, **106**, 9122–9125.
54 B. Hu, R. Shu, Z. Tian, C. Wang, Y. Chen and Y. Xu, Enhancement of hydrogen production via methanol steam reforming using a Ni-based catalyst supported by spongy mesoporous alumina, *Green Chem.*, 2024, **26**, 5485–5498.
55 M. Xiao, A. Baktash, M. Lyu, G. Zhao, Y. Jin and L. Wang, Unveiling the role of water in heterogeneous photocatalysis of methanol conversion for efficient hydrogen production, *Angew. Chem., Int. Ed.*, 2024, **63**, e202402004.